RESEARCH ARTICLE

Key Points:
- Climatology and linear trend of seasonal water temperature in a coastal sea connected to the Kuroshio are investigated
- Air-sea heat flux plays a dominant role in warming of winter-time water temperature
- Oceanic heat transports are responsible for enhanced cooling in spring

Correspondence to:
E. Tsutsumi,
tsutsumi@riam.kyushu-u.ac.jp

Climatology and linear trends of seasonal water temperature and heat budget in a semienclosed sea connected to the Kuroshio region

Eisuke Tsutsumi[1,2] and Xinyu Guo[2]

[1]Research Institute of Applied Mechanics, Kyushu University, Fukuoka, Japan, [2]Center for Marine Environmental Studies, Ehime University, Matsuyama, Japan

Abstract The climatology and linear trend of seasonal water temperature and heat budget in a semienclosed sea connected to the Kuroshio region (Seto Inland Sea: SIS) are investigated by constructing and analyzing a gridded data set of water temperature, salinity, and air-sea heat fluxes. In the SIS, winter-time water temperature and ocean heat content (*OHC*) showed a significant increasing trend while those in summer-time exhibited no significant change. By analyzing the heat budget between the tendency of ocean heat content $\partial OHC/\partial t$ and air-sea net heat flux Q_{net}, the driving factor of the winter-time warming trend in the SIS was identified as autumn Q_{net}, while the unchanged summer-time *OHC* is mainly due to decreased spring-time oceanic heat transport to the SIS from the Kuroshio region. In addition, we showed that the decreased spring-time heat transport could have been induced by upwelling due to wind curl and wind speed in the shelf-slope region, heat transport by the Kuroshio south of Shikoku Island, and freshwater input to the SIS from rivers. The importance of both oceanic and atmospheric forcing mechanisms for explaining variation in the water temperature in coastal areas is demonstrated.

1. Introduction

The upper ocean temperature, especially sea surface temperature (SST), impacts climate variability both in the ocean and atmosphere through the air-sea exchange of heat, fresh water, carbon dioxide, and so on. The upper ocean warmed globally over the period 1971–2010, with an average warming rate in the upper 75 m of +0.11°C per decade [*Rhein et al.*, 2013], but the rate of change exhibits temporal and spatial variability.

Rapid warming (0.3–0.5°C per decade) in semienclosed and shelf seas over the world as well as in the Kuroshio Current during a period of 1982–2006 has been reported by *Belkin* [2009], who investigated SST changes since 1951 in all coastal areas in the world ocean. Similarly, many warming phenomena in SSTs over the past 30 years have been detected in the world-wide coastal area (0.18°C per decade, on average) by *Lima and Wethey* [2012]. They indicated the warming rate has been heterogeneous in both space and seasonality, and the seasonality of SST warming is extremely important for coastal marine ecosystems. Mechanisms causing the seasonality in the warming rate however remains a challenge in each area.

High warming rates for SSTs have also been found over the global western boundary currents [*Wu et al.*, 2012]. Over the Kuroshio in the northwestern Pacific, mean SST warming rate over the period 1900–2008 (1950–2008) is 1.29 (1.10)°C per century, which is significantly higher than the global mean, 0.62 (0.71)°C per century [*Wu et al.*, 2012].

In the inner (onshore) region of the Kuroshio, the warming rate of the water temperature has been observed to be higher in winter than in summer. In the East China Sea (Bohai and Yellow Seas), the winter-time SST trend was 0.38 (0.27)°C per decade over the period 1962–2011, while the summer-time one was 0.18 (0.12)°C per decade [*Bao and Ren*, 2014]. In Taiwan Strait, *Belkin and Lee* [2014] reported that the long-term SST warming during 1957–2011 is strongest in winter (0.7°C per decade) and weakest in summer (0.2°C per decade). In the Tsushima Warm Current, which is a branch of the Kuroshio, the winter-time water temperature increased 0.4–1.3°C over the period 1971–2000, while the change in the summer-time water temperature was insignificant [*Senjyu et al.*, 2010]. In a semienclosed bay near the Tsushima Warm Current,

Takashige et al. [2013] showed that the winter(summer)-time SST trend was about $0.03(-0.02)$°C yr^{-1} over the period 1955–1995. *Kondo et al.* [2005] found that the winter(summer)-time SST changed by 0.4–1.3 (-1.2 to -0.7)°C over the period 1975–2001 in a bay connected to the Tsushima Warm Current region. In the Seto Inland Sea (SIS), which is a semienclosed bay connected to the Kuroshio region, *Takahashi and Seiki* [2004] showed that an average increase of approximately 1°C was detected in winter in the water temperature at 10 m depth over the period 1972–2001 over the whole of the SIS, compared to insignificant changes in the summer-time water temperature.

In the aforementioned studies, several mechanisms have been proposed to explain the trends in the water temperature. *Bao and Ren* [2014] showed winter monsoon intensity was well correlated with the winter-time SST in the China marginal seas while summer monsoon had less effect on the summer-time one. *Belkin and Lee* [2014] discussed relations between the winter amplification of long-term SST warming in the Taiwan Strait and intensification of the winter monsoon. *Senjyu et al.* [2010] suggested a relationship between inter-decadal temperature variation and the Pacific Decadal Oscillation. *Takashige et al.* [2013] indicated the summer-time cooling trend was due to atmospheric forcing while *Kondo et al.* [2005] concluded the summer-time cooling trend was explained by oceanic water exchange with the Tsushima Warm Current region. Although these studies showed seasonality in the linear trend of the water temperature and their possible driving mechanisms, none of them considered both atmospheric and oceanic effects in a quantitative way.

The heat budget has also been examined to determine the drivers for temperature trends. In the East China Sea, a significant contribution to oceanic heat transport by the Kuroshio has been reported [*Kondo*, 1976; *Liu et al.*, 2010]. In the SIS, *Tawara* [1986] and *Murakami et al.* [1989] investigated the seasonal variation of the heat budget using in situ data and a numerical model, respectively. Both studies concluded that the surface heat flux was dominant in the heat budget in the SIS in summer and autumn but warm water transport from the open ocean was also significant in winter and spring. However, in their studies, there were uncertainties in their estimations of the surface heat flux and the long-term variation of the heat budget was not investigated.

Here we present an investigation of the linear trend of water temperature and heat budget in the SIS and its connecting channels by constructing and analyzing data sets of water temperature and air-sea heat fluxes. The SIS is a typical coastal sea and its hydrographic condition is considered to be highly affected by the Kuroshio, and it therefore presents a good case study for understanding the mechanisms controlling water temperatures in coastal seas. Special emphasis is placed on the seasonality in linear trends of water temperature and both atmospheric and oceanic forcing.

The SIS is surrounded by the islands of Shikoku, Honshu and Kyushu and consists of several subbasins and straits (Nada and Seto in Japanese, respectively), as shown in Figure 1. We define the area including Iyo-Nada, Suo-Nada, Aki-Nada, Hiuchi-Nada, Bisan-Seto, Harima-Nada, and Osaka Bay as the SIS. The SIS connects to the open ocean through western and eastern channels; the Bungo and Kii channels, respectively. We also define the 200 m depth isobaths south of the SIS as the location of the shelf edge (white line in Figure 1) and refer to the area south of the shelf edge as the Kuroshio region. Specifically, we refer to the area between the average northern and southern edges of the Kuroshio (dotted lines in Figure 1) and the area between the shelf edge and the northern edge of the Kuroshio as the Kuroshio and shelf-slope region, respectively (for the definition of the average Kuroshio edges, see Appendix A).

2. Data

2.1. Data Sources

For the analysis of sea water temperature and salinity (T-S) in the SIS, we used in situ hydrographic data constructed by *Takahashi and Seiki* [2004, hereinafter TS04], as well as archived data from the Japan Oceanographic Data Center (JODC; http://www.jodc.go.jp) and in situ data from the Japan Meteorological Agency (hereinafter, JMAs; http://www.data.jma.go.jp/kaiyou/db/vessel_obs/data-report/html/ship/efile_NoS2.html). The TS04 data set consists of monthly regular samplings conducted by the Prefectural Fisheries Experiment Stations in the SIS (Figure 2a; blue filled circles). The JODC data are a compilation of in situ measurements made around the Japanese islands by various organizations including universities and the Prefectural Fisheries Experiment Stations (Figure 2a; gray filled circle), but not the JMA. Therefore, the JODC
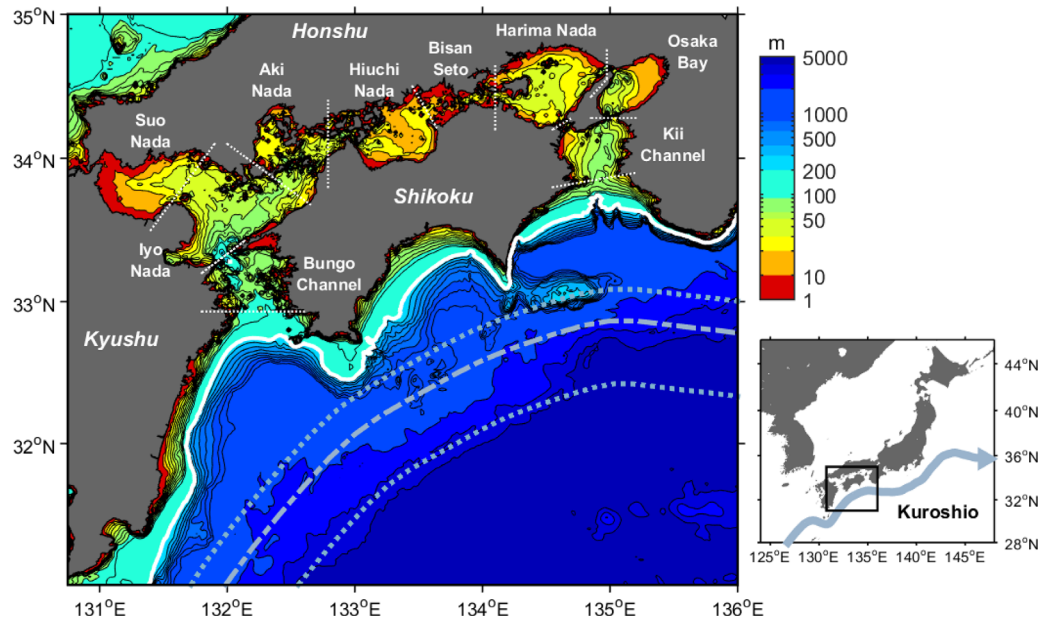
Figure 1. (left) Bathymetric map of the Seto Inland Sea (color shade) and the boundaries between basins (Nada in Japanese), straits (Seto), bays, and channels (white dashed line). Bathymetry is based on the 500 m grid depth data from the Japan Oceanographic Data Center. The thick white line denotes the shelf edge at 200 m depth isobaths south of the channels. Dot-dashed and dot gray curves show the climatological mean Kuroshio path and the northern and southern edges over the period 1964–2001. (right) Map showing the locations of the Seto Inland Sea (square) and the average Kuroshio path (gray curve).

data set includes many observations identical to the TS04. We extracted these duplicate observations from the JODC data set, and utilizing them, cross checked and corrected the TS04 data. The JMA data set is very small compared to the other two sources, but its regularly sampled, seasonal data may provide useful information about the Kuroshio region (Figure 2a). Most of these data were sampled around the reference
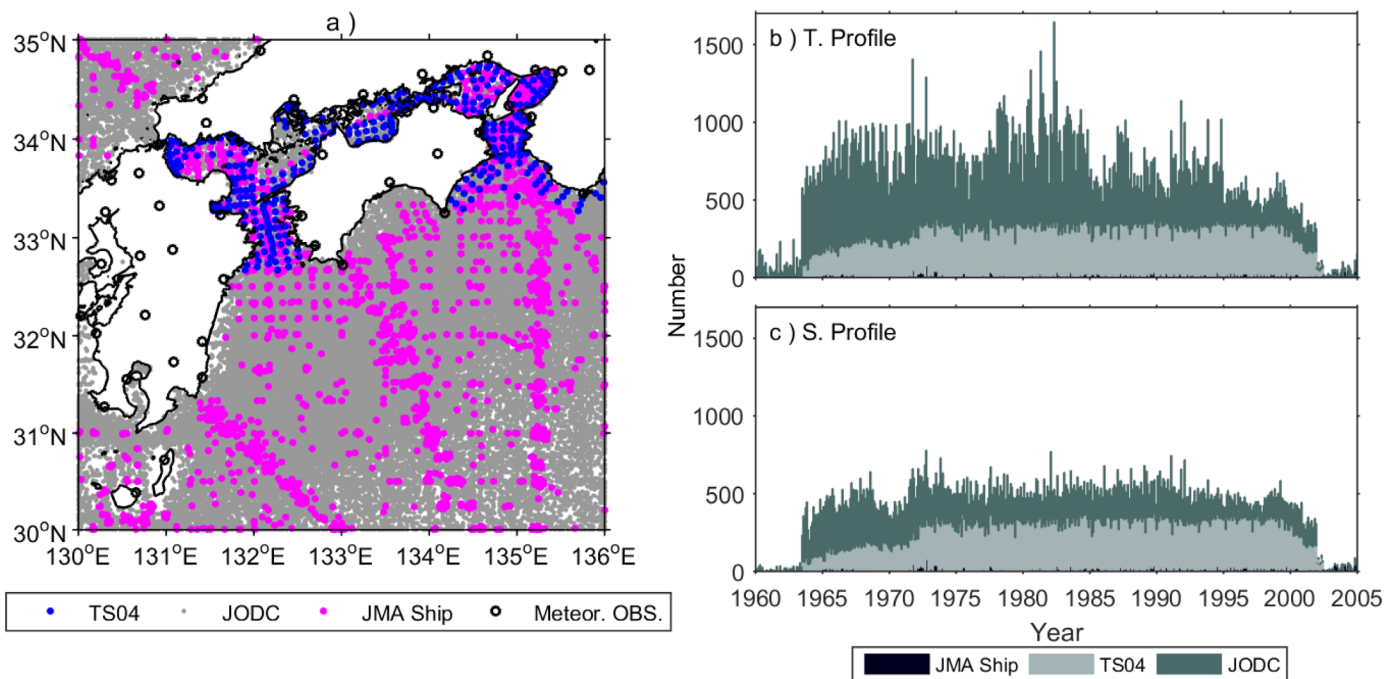
Figure 2. (a) Map showing the position of the in situ data of *Takahashi and Seiki* [2004] (TS04; blue dot), the Japan Oceanographic Data Center (JODC; gray dot), and the Japan Meteorological Agency ship (JMA ship; magenta dot). Positions of the JMA meteorological observatories are also shown with open circles. Monthly time series of the cumulative number of temperature and salinity profiles are shown in Figures 2b and 2c, respectively.

depths: 0, 10, 20, 30, 50, 75, 100, 150, 200, 300, 500, 1000, 2000, 3000, 4000, 5000 m, and near the seabed. We used the JODC and JMA data within 130°E–136°E, 30°N–35°N and all of the TS04 data to construct a gridded data set of temperature and salinity for objective analysis as described below. We selected 1964–2001 for our analysis period, as this provided the best coverage from the T-S data (Figures 2b and 2c).

For the calculation of air-sea heat fluxes, we used daily-average global solar radiation and the rate of cloud cover observed at the observation stations of the JMA shown in Figure 2a (open circles) as well as surface air temperature (SAT), relative humidity, sea level pressure, and surface wind from two reanalysis products by the JMA; Japanese 55 year reanalysis (JRA-55) [Kobayashi et al., 2015] and mesoscale-model grid point values (MSM-GPV). Because the MSM-GPV has a fine spatial resolution (∼5 km horizontally) but short temporal coverage (2006–2013), while the JRA-55 has a long coverage period (1955–2013) but relatively coarse resolution (∼1/2° horizontally), we reconstructed daily-average atmospheric data over the period 1964–2001 with linear regression of the JRA-55 data on the MSM-GPV data for the overlapping period of the two data sets. Correlation coefficients between the reconstructed data set and the MSM-GPV for the period 2006–2013 are generally high ($r > 0.8$). The reconstructed data are linearly interpolated onto the ocean grid, while the cloud cover rate is interpolated using an exponential filter whose parameters are determined from the covariance of the data.

2.2. Gridding Method for Seawater Temperature and Salinity

To obtain the three-dimensional distribution (longitude, latitude, and depth below the sea surface) of the monthly average T-S, an objective analysis method was applied to the in situ observation data noted in section 2.1. The bathymetry in the SIS and the Kuroshio region are gridded at 0.02° intervals over 30°N–35°N and 130°E–136°E using 500 m mesh depth data produced by the JODC (shown in Figure 1), and then grid point values of T-S are obtained with the following method.

Analysis data of monthly temperature and salinity were obtained with a standard optimal interpolation method [Bretherton et al., 1976]; analysis $\mathbf{x}^a$ is calculated from observation $\mathbf{y}^o$ and the first guess $\mathbf{x}^b$ by $\mathbf{x}^a = \mathbf{x}^b + \mathbf{K}(\mathbf{y}^o - \mathbf{Hx}^b)$, where $\mathbf{K}$ and $\mathbf{H}$ are a weight for optimal interpolation and an operator which functions as the bilinear interpolation from the observation points onto the grid points, respectively. We use persistence-based prediction for $\mathbf{x}^b$; $\mathbf{x}^b_n = \mathbf{x}^{clim}_n + \alpha(\mathbf{x}^a_{n-1} - \mathbf{x}^{clim}_{n-1})$, where superscript "clim" and subscript "n" represent monthly climatology and calendar month, respectively [Smith, 1995]. The autocorrelation coefficients for a 1 month lag, α, are set to 0.5 based on the evaluation using the in situ data. The weight $\mathbf{K}$ is defined as $\mathbf{K} = \mathbf{P}^{go}(\mathbf{P}^{oo} + \mathbf{R})$ using covariance matrices $\mathbf{P}^{go}$ and $\mathbf{P}^{oo}$ where the covariance between two points k, l is modeled as a function of distance d_{kl} by $P_{kl} = P_1 \exp(-d_{kl}/L) + P_0$ at each depth. Parameters L, P_0, and P_1 are determined by fitting the model to the covariance of the in situ data. The observation error $\mathbf{R}$ was given by the variability of T-S in each month. In general, most of the in situ data are sampled in the first week of each month so that we simply set the time of the respective monthly analyses to the first day of a month.

2.3. Air-Sea Heat Fluxes

The net air-sea heat flux Q_{net} is defined as

$$Q_{net} = Q_s + Q_b + Q_h + Q_e \tag{1}$$

where Q_s, Q_b, Q_h, and Q_e are shortwave radiation, longwave back radiation, and sensible and latent heat fluxes, respectively. All fluxes are defined to be positive if they are seaward. Shortwave and longwave radiative fluxes are estimated using a standard and Clark et al. [1974] formulae, respectively:

$$Q_s = (1-\alpha)I_g \tag{2}$$

$$Q_b = -\varepsilon \sigma T_s^4 (0.39 - 0.05 e_a^{1/2})(1 - \delta n_c^2) - 4\varepsilon \sigma T_s^3 (T_s - T_a) \tag{3}$$

where I_g is the global solar radiation in W m^{-2}, α is the sea surface albedo that is assumed to be highest in winter and lowest in summer (= 0.06–0.1) [Tawara, 1986], ε is the emissivity of sea surface (= 0.97), σ is the Stefan-Boltzmann constant (= 5.67×10^{-8} W m^{-2} K^{-4}), e_a is vapor pressure in hPa, δ is the cloud coefficient (= 0.65), n_c is the cloud cover rate (as a decimal proportion of one) and T_s and T_a are SST and SAT in K, respectively.

Sensible and latent heat fluxes are calculated using the following bulk formulae:

$$Q_h = \rho_a c_a c_h (T_a - T_s)|\mathbf{V}| \tag{4}$$

$$Q_e = \rho_a L c_e (q_a - q_s)|\mathbf{V}| \tag{5}$$

where ρ_a is the air density in kg m^{-3}, c_a is the specific heat capacity of the air in J kg^{-1} K^{-1}, L is the latent heat of evaporation in J kg^{-1}, q_s and q_a are the vapor pressure at the sea surface and the surface air in hPa, respectively, and $\mathbf{V}$ is the surface wind vector in m s^{-1}. The bulk coefficients c_h and c_e in equations (4) and (5), respectively, are determined according to *Kondo* [1975].

Daily values of these fluxes were calculated first from the daily atmospheric data and daily SST that were obtained by linear interpolation from the monthly SST, and their monthly average was defined at the middle day of a month. In this study, shortwave radiation is assumed to be spatially uniform and calculated using the global solar radiation data over 18–40 (varies in time) observation stations located in western Japan.

3. Climatology

We first show climatological features of water temperature and air-sea heat fluxes and confirm the mechanisms for heat fluxes to the SIS in each season. Hereinafter, we refer to December, January, and February as winter, March, April, and May as spring, June, July, and August as summer, and September, October, and November as autumn. We choose these "terrestrial" seasons because, as we will show in section 3.3, seasonal heat budget in the SIS is strongly affected by net air-sea heat flux and its seasonal variation is close to terrestrial one rather than to "oceanic" one (i.e., January, February, and March as winter, . . .). Also, we use the terrestrial seasons because seasonal contrast of linear trends of terrestrial-seasonally averaged water temperature and heat budget is more significant than that with the oceanic seasons.
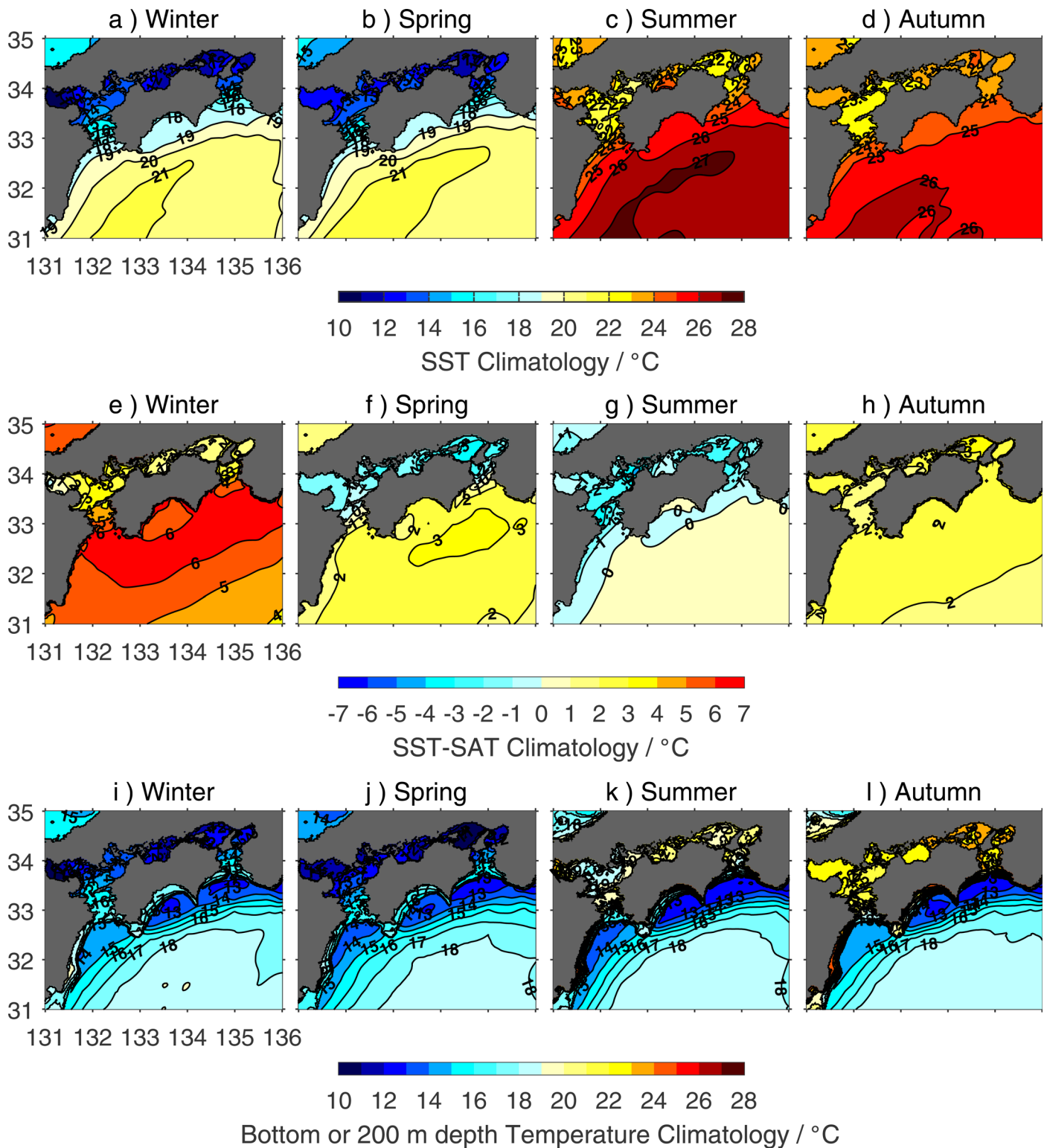
3.1. Water Temperature and Air-Sea Temperature Difference

Figures 3a–3d show the seasonal average SST. In the SIS and the channels, water temperature is generally lowest in March and highest in August or September throughout the water column. In winter and spring, thermal fronts are formed between the cold (<15°C), shallow inland sea and the warm (20–21°C), deep Kuroshio water. In summer, the temperature of the SIS and the channels is lower than in the Kuroshio region, partly due to strong tidal mixing in the narrow straits. This is evident from the frequent formation of tidal fronts in the SIS and the Bungo Channel [*Yanagi*, 1987; *Takeoka et al.*, 1993; *Takeoka et al.*, 1997]. In autumn, these frontal structures are relatively relaxed. The seasonally varying SST gradient in the SIS is consistent with that found in the latest regional climatology of the East Asian Seas [*Johnson and Boyer*, 2015]. The water temperature in the SIS is thus generally lower than the surface temperature in the Kuroshio region throughout the year.

The air-sea surface temperature difference, which plays a key role in air-sea heat exchange, is affected mainly by the SST structure (Figures 3e–3h). In spring and summer (autumn and winter), the SST in the SIS is higher (lower) by 1–3°C than the surface air temperature (SAT) at the same position. In the Kuroshio region, the SST is generally higher than the SAT throughout the year because of the large amount of meridional heat transport by the Kuroshio Current.

In the SIS and its channels, the water column is vertically homogeneous in winter and autumn and stratified in spring and summer. The temperature at the bottom in the SIS and the channels is significantly lower in summer (2–5°C) than the SST but not so different in the other seasons (< 1°C) (Figures 3i–3l). A striking feature of the water temperature at 200 m depth can be seen in the shelf-slope region: it is significantly colder (<15°C) than at the bottom of the channels and at 200 m depth south of the Kuroshio throughout the year (Figures 3i–3l). It forms a band structure along the Kuroshio.

Such subsurface cold water exists along the shelf-slope throughout the year. This is evident from the thermal structure across the Kuroshio (lines A and B in Figure 4). In both sections, isotherms are located at a shallower depth on the inshore side of the Kuroshio than on the offshore side. This is mainly due to dynamical isotherm uplift caused by geostrophic adjustment related to the Kuroshio, which has been commonly observed in the western boundary current systems [e.g., *Shen et al.*, 2011]. In addition, the horizontal

Figure 3. Seasonal climatological map of the (a–d) sea surface temperature, (e–h) the air-sea surface temperature difference, and (i–l) the seabed or 200 m depth water temperature. Solid and dashed white lines in the bottom plots show the 200 m depth isobaths and the average Kuroshio edges, respectively.

gradient of subsurface (around 200 m depth) temperature across the northern edge of the Kuroshio is relaxed in spring and strengthened in summer or autumn (Figure 4). This fact is dynamically consistent with the seasonal variation of the Kuroshio transport south of Shikoku reported by *Kakinoki et al.* [2008], which is
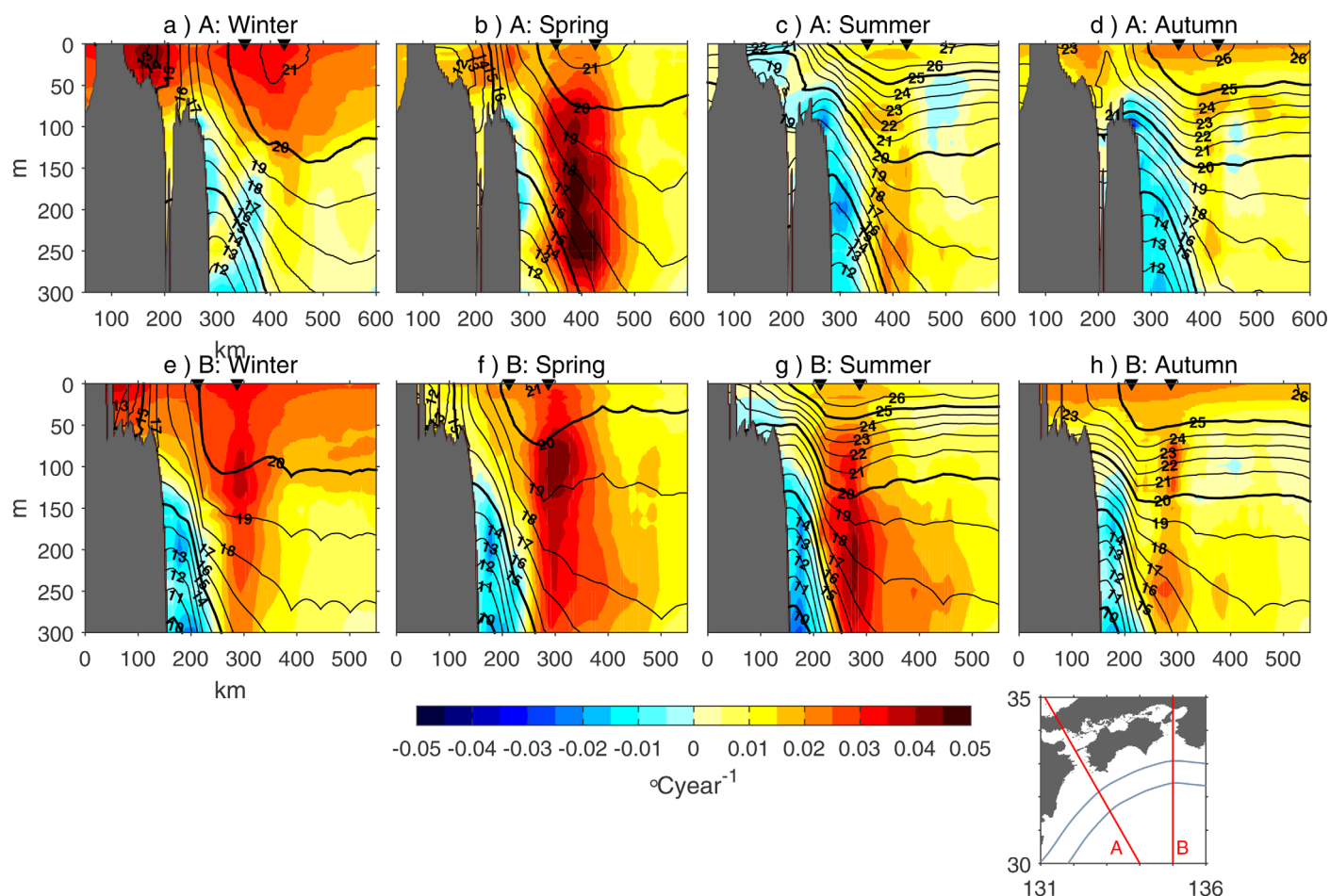
Figure 4. Climatology (solid line) and linear trend (color shade) of seasonal water temperature in °C at vertical sections along the lines (a–d) A and (e–h) B that are shown in the bottom-right plot. In Figures 4a–4h, black filled triangles indicate the location of the Kuroshio edges shown in the bottom-right plot by gray solid line.

at its minimum in March and maximum in September. It should be noted that SST gradient across the Kuroshio front becomes weak in summer to autumn south of the SIS (Figures 3a–3d), which is consistent with the reported seasonal variation of the Kuroshio front in the East China Sea [e.g., *Hickox et al.*, 2000].

3.2. Heat Fluxes

Figures 5a and 5b shows the monthly climatology of the net air-sea heat flux and its components averaged over the SIS and the two channels, respectively. The maximal heating of 176 W m^{-2} in the SIS and 187 W m^{-2} in the channels occurs in July and the maximal cooling of −149 W m^{-2} in the SIS and −213 W m^{-2} in the channels is in December. The turbulent heat flux, $Q_h + Q_e$, in the SIS and the channels in summer is quite small because of weak winds and small air/sea vapor pressure difference, q_a–q_s (figure not shown). The difference in the heat flux between the SIS and the channels is not so large, but the turbulent heat flux during late autumn to winter is larger in the channels by 40–90 W m^{-2} than in the SIS, which is due to the large SST-SAT difference (Figure 3e) and stronger northerly winds (figure not shown) in the channels.

To assess our heat flux calculations, a comparison with previously reported heat fluxes is made in Table 1. *Tawara* [1986] estimated the heat fluxes using in situ SST and meteorological data over the SIS and the channels, *Murakami et al.* [1989] estimated the heat fluxes in the SIS and the channels using in situ meteorological data and calculated the SST with a simple numerical model, and *Chang et al.* [2009] estimated the heat flux using in situ atmospheric and oceanic data at a central station in the SIS. Because there are no significant differences among the shortwave radiation of individual studies including ours, we compared the net fluxes and the other components (Q_b, Q_e and Q_h).
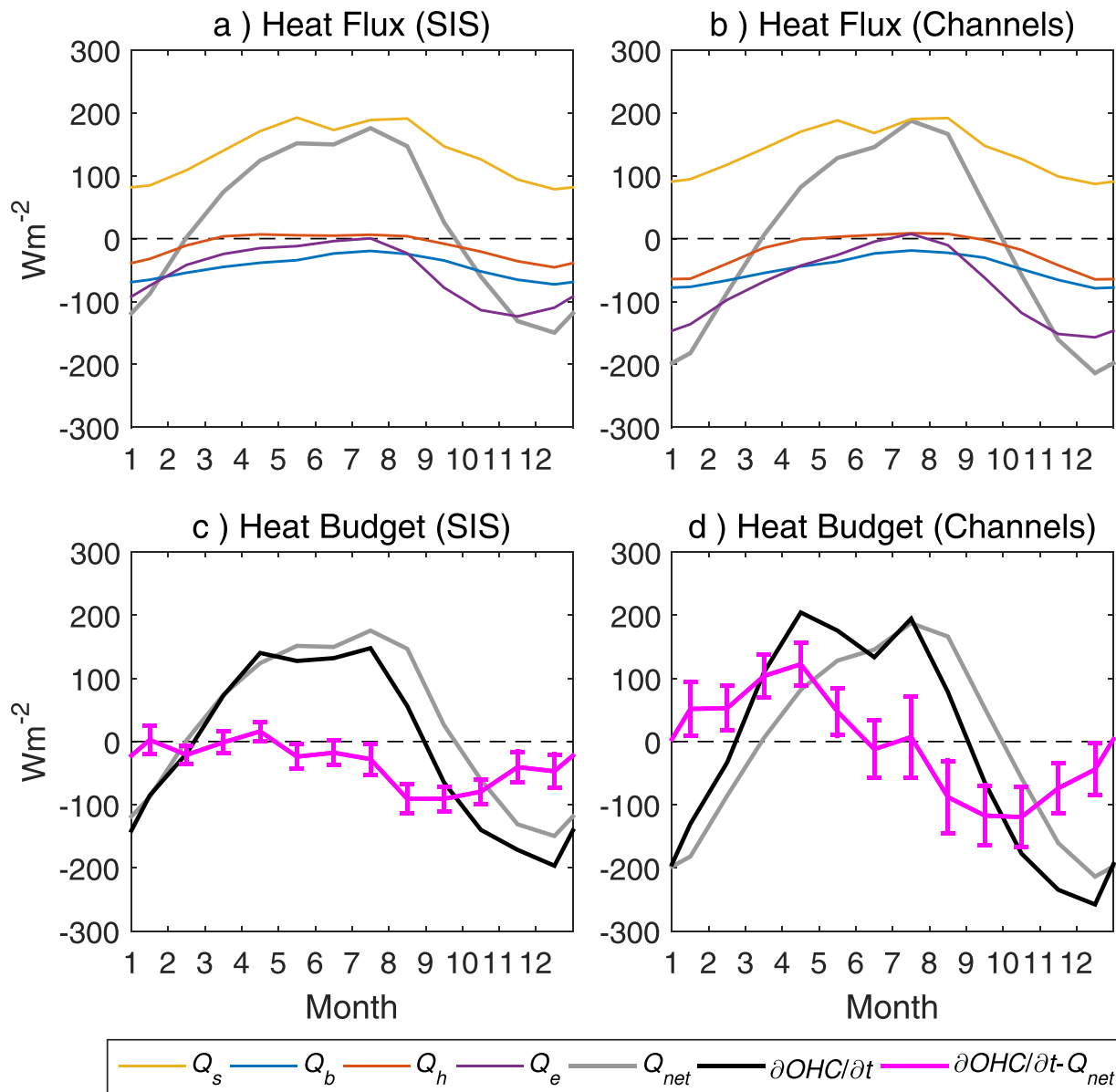
Figure 5. Monthly climatological (top) air-sea heat fluxes and (bottom) heat budget averaged over (a, c) the Seto Inland Sea (SIS) and (b, d) sum of the Bungo Channel and the Kii Channel (Channels). $\partial OHC/\partial t$ is the tendency of ocean heat content and Q_s, Q_b, Q_h, Q_e, and Q_{net} are shortwave radiation, longwave radiation, sensible heat flux, latent heat flux, and net heat flux, respectively, where $Q_{net} = Q_s + Q_b + Q_h + Q_e$. Error bars in the bottom plots show one standard deviation.

Using the estimates from the present study as a reference, the root-mean-square error (RMSE) and mean error (ME) for the reported heat fluxes are calculated (Table 1). The net heat flux of *Tawara* [1986] and *Murakami et al.* [1989] appeared to be much lower than that of the present study both in the SIS and in the channels (ME = −144.6 to −68.9 W m^{-2}). The comparison with the heat fluxes of *Chang et al.* [2009] is relatively similar (ME = −30.3 in Q_{net}). The difference between our calculation and that of *Tawara* [1986] and *Murakami et al.* [1989] could arise from the bulk coefficient for the latent flux and the monthly values of T_s, T_a and **V** used in both *Tawara* [1986] and *Murakami et al.* [1989]. In these studies, they used an empirical constant of bulk coefficient for the latent heat flux ($c_e = 2.0 \times 10^{-3}$) proposed by *Ishizaki and Saito* [1978]. It is larger, especially in summer, than the typical value of Kondo's bulk coefficient that would fully account for the effect of surface air stability. In addition, usage of monthly averaged SST, SAT and wind in *Tawara* [1986] and *Murakami et al.* [1989] could introduce errors by ignoring covariance between wind and SST or SAT [*Hirose et al.*, 1999].

Table 1. Heat Fluxes in the SIS and Channels. RSME and ME are Root Mean Squared Error and Mean Error, Respectively

		Jan	Feb	Mar	Apr	May	Jun	Jul	Aug	Sep	Oct	Nov	Dec	unit: RMSE	Wm^{-2} ME
Tawara 1986	Q^{net}	−237.2	−133.1	−53.5	45.3	86.5	80.5	116.6	71.3	−55.6	−161.6	−210.9	−253.8	98.3	−94.1
(SIS)[a]	Q_b	−76.4	−71.7	−65.6	−45.6	−40.0	−29.7	−18.8	−22.7	−39.9	−65.1	−76.4	−77.7	10.6	−8.4
	Q_e	−155.7	−125.4	−112.2	−71.0	−72.8	−70.9	−64.5	−112.6	−153.7	−191.5	−181.0	−180.3	73.5	−72.7
	Q_h	−81.8	−56.0	−30.8	2.8	10.9	7.2	17.0	12.7	−14.1	−41.1	−57.7	−78.1	25.8	−15.6
Tawara 1986	Q_{net}	−477.2	−313.4	−197.0	−20.8	37.6	83.3	167.3	72.7	−58.4	−220.9	−315.0	−423.1	163.2	−144.6
(Channels)[a]	Q_b	−82.7	−78.1	−69.7	−47.5	−38.4	−25.5	−13.8	−20.6	−35.7	−60.3	−77.8	−81.5	8.1	−5.5
	Q_e	−339.7	−250.6	−214.7	−126.7	−117.0	−73.0	−33.4	−111.7	−160.9	−239.8	−262.5	−303.8	121.4	−113.9
	Q_h	−159.6	−111.2	−67.4	−9.2	6.1	12.5	29.9	20.0	−9.7	−49.5	−80.2	−126.7	44.9	27.1
Murakami et al. 1989	Q_{net}	−165	−103	−52	41	93	114	145	103	−21	−145	−248	−237	73.5	−68.9
(SIS+Channels)[b]															
Chang et al. 2009	Q_{net}	−100	−35	45	95	115	115	140	90	−25	−95	−140	−145	34.4	−30.3
(SIS)[c]	Q_b	−60	−50	−40	−40	−35	−30	−30	−35	−45	−70	−75	−75	9.5	−4.7
	Q_e	−110	−90	−65	−55	−45	−40	−40	−80	−125	−135	−135	−125	37.7	−35.4
	Q_h	−20	−10	0	5	5	5	5	0	−10	−15	−20	−25	8.6	3.5
Present study	Q_{net}	−87.5	2.5	74.5	124.3	151.5	149.7	175.6	146.9	25.9	−60.3	−130.9	−149.3		
(SIS)	Q_b	−65.1	−54.0	−44.8	−38.3	−34.3	−23.7	−19.5	−24.5	−34.7	−51.9	−65.1	−72.5		
	Q_e	−74.7	−41.7	−24.3	−15.0	−11.9	−4.0	0.4	−23.3	−77.9	−113.7	−123.7	−109.8		
	Q_h	−32.1	−10.6	3.8	6.8	5.4	4.7	6.2	3.8	−8.2	−20.6	−35.9	−45.6		
Present study	Q_{net}	−181.6	−85.6	5.9	82.0	128.2	145.6	187.4	166.3	53.3	−57.1	−160.2	−213.3		
(Channels)	Q_b	−76.4	−66.2	−54.6	−44.2	−36.8	−23.6	−18.9	−22.5	−30.2	−48.2	−65.3	−78.6		
	Q_e	−136.0	−97.3	−68.3	−42.9	−26.0	−4.7	7.5	−10.4	−62.1	−117.8	−151.6	−156.9		
	Q_h	−63.7	−39.6	−14.6	−1.0	2.9	5.9	8.6	7.5	−1.9	−17.8	−42.2	−64.7		
Present study	Q_{net}	−106.6	−15.4	60.5	115.7	146.8	148.9	178.0	150.8	31.4	−59.6	−136.8	−162.3		
(SIS+Channels)															

[a]RSME and ME are root-mean-squared error and mean error, respectively.
[b]From Tawara [1986, Table 8].
[c]From Murakami et al. [1989, Figure 6a].
[d]From Chang et al. [2009, Figure 4].
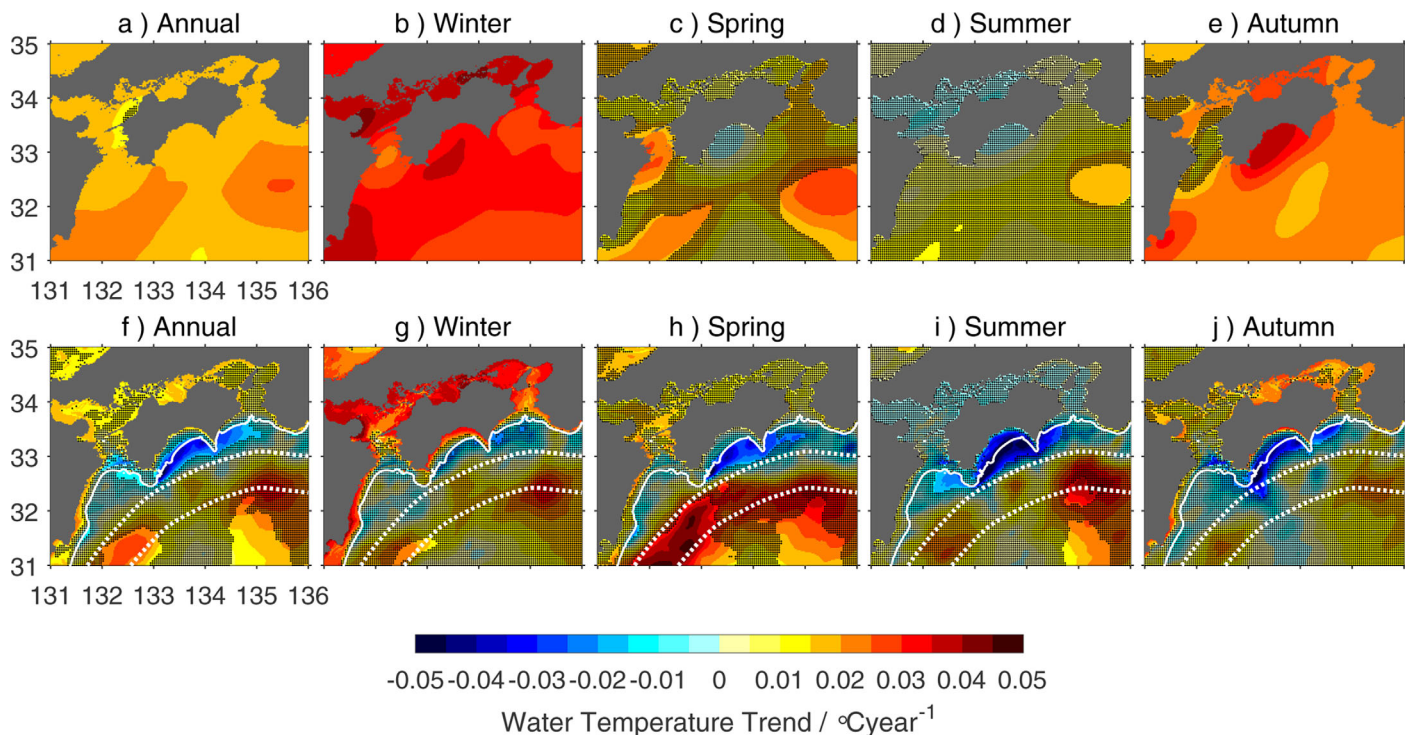
Figure 6. Linear trend for annual and seasonally averaged water temperature anomaly (a–e) at the sea surface and (f–j) at the seabed or 200 m depth. Solid and dashed white lines are the same as in Figures 3i–3l. Dark shading is overlaid on the region where the trend is not significant at the 95% significance level.

In fact, the winter-time turbulent heat flux of -400 W m^{-2} and the summer-time flux of -100 W m^{-2} approach or exceed typical values above the Kuroshio [e.g., *Kida et al.*, 2015], and therefore are likely too large for the values in the channels and the SIS which are distant from the Kuroshio. Relatively good correspondence with the heat fluxes by *Chang et al.* [2009], who use *Kondo's* [1975] bulk coefficients with daily SST, SAT and wind, implies a reproducibility of our flux estimation. Although there are many uncertainties in our flux estimation, such as uncertainties in the reanalysis data, in the reconstruction method, from not accounting for hourly covariance between SST and wind, and so on, the above studies do not contradict the results of our calculations.

3.3. Heat Budget

In the SIS and the channels, the rate of change of the OHC is assumed to be controlled by air-sea heat fluxes Q_{net} and the divergence of horizontal transport of OHC by ocean currents Q_v, that is,

$$\frac{\partial OHC}{\partial t} = Q_{net} + Q_v \tag{6}$$

where $OHC = \int_{-H}^{0} \rho_s c_p \theta dz$, ρ_s and θ are the potential density of water and the potential temperature of seawater, respectively, c_p is the specific heat capacity of seawater ($= 4020$ J kg^{-1} K^{-1}), and H is the water depth [e.g., *Stewart*, 2008]. Note that H is set to 200 m in the area in which the water depth is greater than 200 m such as the Kuroshio region. The tendency of OHC in a calendar month n is calculated as $(OHC(n+1) - OHC(n))/\Delta t(n)$, where $\Delta t(n)$ is the time in terms of month n. All terms in equation (6) are defined at the middle of the month.

In the SIS, $\partial OHC/\partial t$, which ranges from -200 W m^{-2} in winter to 130 W m^{-2} in summer, is dominated by Q_{net} in winter and spring, while the influence of horizontal heat transport Q_v ($= \partial OHC/\partial t - Q_{net}$) becomes greater ($-100$ to -50 W m^{-2}) from summer to autumn (Figure 5c). This means that water temperature in the SIS is reduced by the outer seawater in summer to autumn. In the channels, spring-time positive heat transport (warming) by ocean currents is also significant (~ 100 W m^{-2}) as well as summer-autumn-time cooling (~ -100 W m^{-2}), exhibiting an annual sinusoidal like variation. It results in a significant peak in April in the tendency of the OHC (Figure 5d).

The summer-time cooling by ocean currents is consistent with many studies on the intrusion of oceanic cold water into the channel and the SIS [e.g., *Takeoka et al.*, 2005; *Sugimatsu and Isobe*, 2010]. The spring-time warming heat flux by the oceanic transport in the channels has not yet been confirmed with observations, but is strongly suggested in numerical simulations by *Chang et al.* [2009], who showed a warm, northward surface current extending from the channels to the SIS with a southward counter current at the bottom in spring.
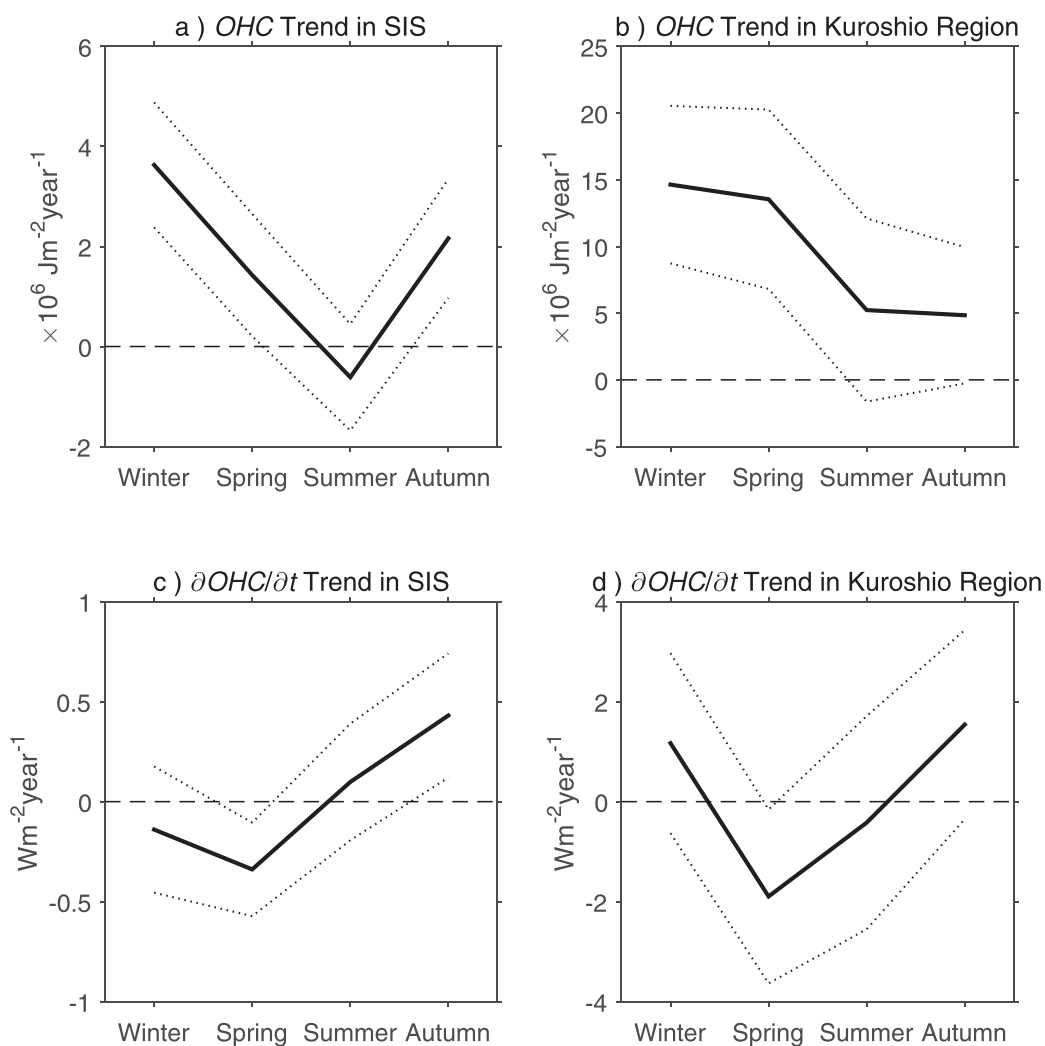
4. Linear Trend

In section 3, we confirmed that our T-S and air-sea heat flux data sets are reasonably consistent with past studies. In this section, we investigate the linear trend of the water temperature and OHC. In this study, we assessed the significance of linear trends by calculating the 95% significance levels using a Student's t test. Due to the relatively short length of the data set (38 years), we must consider that the linear trends presented below may be a result of inter-decadal and longer variabilities, rather than long-term changes in the climate.

4.1. Water Temperature

Figure 6 shows the linear trend of annual and seasonally averaged water temperature anomalies at the sea surface (a–e) and bottom or 200 m depth (f–j). The linear trend of the annual averaged SST is 0.01–0.02°C yr^{-1} in the SIS, the channels and the Kuroshio region, all of which are judged as statistically significant at the 95% significance level. This is roughly consistent with the reported value above the Kuroshio Current by *Wu et al.* [2012] of 1.10 ± 0.31°C per century over the period 1950–2008.

The linear trend of SST shows obvious seasonality as reported by many studies: in autumn and winter, most of the rates of warming for the SST are relatively high at 0.02–0.03°C yr^{-1} and statistically significant over the SIS, the channels and the Kuroshio region. On the other hand, in spring and summer, SST trends in these areas are generally small and most of them are statistically insignificant. For the bottom temperature

Figure 7. Linear trend (solid line) and the 95% confidence limits (dotted lines) of (a, b) ocean heat content (*OHC*) and (c, d) its time derivative (∂*OHC*/∂*t*) in the SIS and the Kuroshio region. *OHC* is defined as heat content in the upper 200 m in the Kuroshio region for the whole water column in the shallower region.

in the SIS and the channel, linear trends are slightly smaller ($<0.005°C\ yr^{-1}$, Figures 6f–6j) and less significant compared to those of the SST.

In the Kuroshio region, most of the linear trends of water temperature at the 200 m depth are insignificant because of its large variability, presumably due to fluctuations in the Kuroshio path. However, the Kuroshio transport and mesoscale eddy activity [e.g., *Qiu and Miao*, 2000; *Book et al.*, 2002; *Miyazawa et al.*, 2004; *Sugimoto and Hanawa*, 2014] show a coherent pattern: water temperature in the shelf-slope region consistently decreases at a rate of -0.04 to $-0.01°C\ yr^{-1}$, especially in spring and summer. Locations where such cooling trends appear are roughly in agreement with the areas where isotherms are uplifted, as seen in Figure 4.

The linear trend of water temperature in the Kuroshio region also shows notable seasonality. A coherent and strong warming trend can be found in the upper 100 m (Figures 4a and 4e) in winter and in the region of the Kuroshio in spring (Figures 4b and 4f), implying warming in winter and spring could be related to atmospheric forcing and Kuroshio variability, respectively. Detailed relationships between these factors and their effect on the SIS will be described in section 5.

4.2. Ocean Heat Content and Its Tendency
The linear trend of ocean heat content in the SIS displays a similar seasonality to that of the water temperature (Figure 7a). *OHC* in the SIS significantly increases in winter ($3.6 \times 10^6\ J\ m^{-2}\ yr^{-1}$) but slightly decreased

(not significant) in summer (-0.6×10^6 J m^{-2} yr^{-1}). The spring-time and autumn-time OHC also increased by 1.7×10^6 and 2.1×10^6 J m^{-2} yr^{-1}, respectively. In the Kuroshio region, seasonality in the linear trend of the upper 200 m OHC is different from that of the SIS (Figure 7b): the linear trend is high in winter and spring (-1.4×10^7 J m^{-2} yr^{-1}) and also positive (but not significant) in summer and autumn (-0.5×10^7 J m^{-2} yr^{-1}). In the channels, seasonality in the OHC trend seems to be a mixture of those in the SIS and the Kuroshio region (figure not shown).

The linear trend of $\partial OHC/\partial t$ in the SIS significantly increases in autumn and decreases in spring, as shown in Figures 8a–8d. This is because the winter-time OHC markedly increases, while that in summer-time is nearly unchanged (Figures 7a and 7c). In spring, the SIS is getting warmer (positive $\partial OHC/\partial t$; Figure 5c) and therefore the negative spring-time $\partial OHC/\partial t$ trend (-0.34 W m^2 yr^{-1}: Figure 7c) means a reduction in the rate of this heating. In autumn, the SIS is cooling (negative $\partial OHC/\partial t$), so the positive autumn-time $\partial OHC/\partial t$ trend (0.43 W m^2 yr^{-1}: Figure 7c) indicates a reduction in the rate of cooling.

In the Kuroshio region, although linear trends of winter-time, summer-time, and autumn-time $\partial OHC/\partial t$ are not significant, the results are similar to those for the SIS in that the spring-time trend is significantly negative (-1.9 W m^2 yr^{-1}: Figure 7d). The positive winter-time trend of $\partial OHC/\partial t$ in the Kuroshio region may be a source of the difference in the OHC trends for the SIS and the Kuroshio region.

4.3. Air-Sea Heat Fluxes and Heat Budget

Air-sea heat flux could be a major driver of the long-term trends in the water temperature. A large linear trend of the net heat flux is seen in the summer-time anomalies for the SIS and the channels (-0.8 W m^2 yr^{-1}) as shown in Figures 8e–8h. Specifically, this positive trend in summer-time Q_{net} in the SIS is due to the enhancement of heating by shortwave and longwave radiation and increased turbulent heat transfer from the air to the sea, $Q_e + Q_h$ (Table 2). In spring and autumn, the situation is similar (0.4–0.5 W m^2 yr^{-1} in the SIS) but the contribution of Q_s to the increased net heat flux is negligible. The trend of winter-time Q_{net} is nearly zero.

Based on the heat balance in equation (6), we can estimate the contribution of the air-sea heat flux to the tendency of OHC quantitatively by $Q_v = \partial OHC/\partial t - Q_{net}$. The pattern in linear trends of Q_v (Figures 8i–8l) is generally similar to that of $\partial OHC/\partial t$ (Figures 8a–8d) in the Kuroshio region because of its large heat content. In the SIS, a significant negative trend of Q_v can be found in spring-time and summer-time (Figures 8j and 8k).

A quantitative comparison between $\partial OHC/\partial t$ and Q_{net} in the SIS is summarized in Table 3. The 7 year running mean autumn-time $\partial OHC/\partial t$ anomaly is well correlated ($r = 0.82$) with that of Q_{net} and their linear trends are almost identical, suggesting the long-term weakening of autumn-time cooling is mainly due to increasing air-sea heat flux. More specifically, it is mainly due to longwave radiation and turbulent heat flux $Q_e + Q_h$ (Table 2).

On the other hand, the correlation of the spring-time $\partial OHC/\partial t$ with Q_{net} anomalies is not significant ($r = -0.07$) and the linear trends have opposite sign to the winter-time trends (positive Q_{net} trend against negative $\partial OHC/\partial t$ trend: Table 3). This suggests that the weakened heating trend in the spring-time SIS could be due to decreased heat transport by ocean currents, Q_v whose trend is estimated as -0.74 W m^{-2} yr^{-1}. In a climatological sense, Q_v in the SIS is nearly zero (Figure 5c), so it is not clear which mechanism is responsible for the decreased Q_v.

The linear trend of summer-time $\partial OHC/\partial t$ (0.10 W m^{-2} yr^{-1}) is not significant but that of Q_{net} is (0.76 W m^{-2} yr^{-1}), indicating a negative linear trend of Q_v (-0.66 W m^{-2} yr^{-1}). In summer, because climatological oceanic heat transport is negative (Figures 5c and 5d), a negative trend of Q_v means stronger cold water transport to the channel and the SIS from the Kuroshio region became stronger. In winter, linear trends of $\partial OHC/\partial t$ and Q_v are both insignificant.

As a brief summary so far, winter-time water temperature and ocean heat content in the SIS and the channels have significantly increased due to weakened cooling by the air-sea heat flux in autumn, while summer-time temperature had not significantly changed presumably due to decreased spring-time oceanic heat transport may have canceled increased heat storage during autumn. In addition, an increasing trend
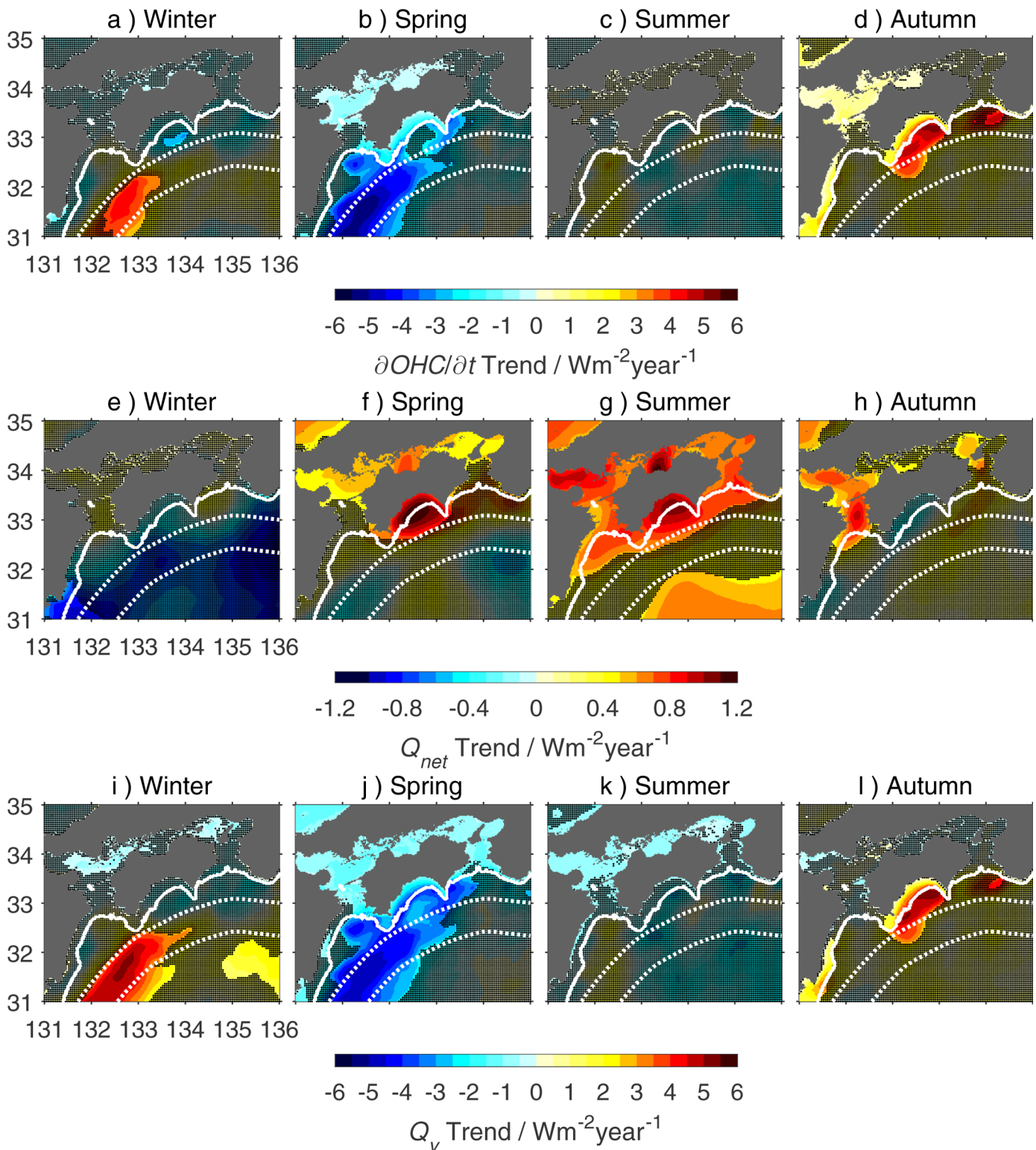
Figure 8. Linear trends of seasonal anomalies of the tendency of the (a–d) ocean heat content $\partial OHC/\partial t$, (e–h) net heat flux Q_{net}, and (i–l) heat transport by ocean currents, $Q_v = \partial OHC/\partial t - Q_{net}$. Shading is overlaid where the trend is statistically insignificant. Solid and dashed white lines in each plot are the same as those in Figures 3i–3l.

of summer-time air-sea heat flux is estimated to have been nearly balanced with the decreasing trend of the summer-time oceanic heat transport. In the following discussion, we focus our scope to the decreased oceanic heat transport in spring and investigate their mechanism.

Table 2. Linear Trend and the 95% Confidence Limits of Seasonal Anomalies of Shortwave Radiation Q_s, Longwave Radiation Q_b, Latent Heat Flux Q_e, and Sensible Heat Flux Q_h in the SIS (Unit: W m^{-2} yr^{-1})

	Q_s	Q_b	Q_e	Q_h
Winter	-0.10 ± 0.22	0.08 ± 0.11	-0.14 ± 0.23	0.17 ± 0.17
Spring	0.05 ± 0.31	0.20 ± 0.09	0.09 ± 0.13	0.06 ± 0.05
Summer	0.30 ± 0.49	0.23 ± 0.09	0.17 ± 0.13	0.06 ± 0.03
Autumn	-0.04 ± 0.22	0.19 ± 0.07	0.14 ± 0.27	0.19 ± 0.09

5. Discussion

5.1. Possible Mechanism Driving Oceanic Heat Transport Into the Spring-Time SIS

Oceanic heat transport to the SIS is largely due to water exchange with the Kuroshio region because the SIS is semi-enclosed and connected primarily to the Kuroshio region. Oceanic heat transport Q_v in the SIS and the channels correlated relatively well with that in the shelf-slope region, as shown in Figure 9. Correlation with the Kuroshio region is higher in spring than other seasons ($r > 0.5$), suggesting that the decreased spring-time oceanic heat transport in the SIS originates from variability in the Kuroshio region.

In spring, water from the shelf-slope region is warmer than that in the channels and the SIS except for the deep layer (Figures 3b, 3j, 4b, and 4f) and it may be transported into the channels and the SIS by density-driven circulations. The change in the horizontal distribution of depth-averaged water density in spring is the generation mechanism for such density currents (Figure 10a): there are strong positive meridional density gradients between the SIS and the slope region (estuarine sense) and negative (inverse-estuarine sense) in the east and west channels, respectively [*Valle-Levinson*, 2010], both of which can drive inshore (offshore) transport of warm (cold) water. Positive air-sea net heat flux in spring (Figures 5a and 5b) also assists density-driven circulations because it reduces vertical eddy diffusivity in the ocean, which plays a central role in maintaining horizontal density gradients [*Valle-Levinson*, 2010]. The existence of such density-driven circulations was confirmed in the numerical simulations by *Chang et al.* [2009].

The density differences between the western and eastern regions of the SIS were mainly due to differences in freshwater input from rivers: river discharge rate into the SIS (obtained from Rainfall/Discharge Rate Database 1938–2003 by the Japan River Association) was generally larger in the eastern part of the SIS than the western part as shown in Figure 11a.

The linear trend of depth-averaged water density shows the meridional density gradient was relaxed in the eastern part of the SIS (Figure 10b), which suggests the spring-time meridional circulation there was weakened. In the Kuroshio region, water density decreased due to increased water temperature but the density decrease was relatively moderate in the shelf-slope region, implying dense (cold) water supplement to the shelf-slope region. Based on the above mechanism, colder water temperature in the shelf-slope region would result in weaker warm water transport to the channel and the SIS because of a decrease in the meridional temperature gradient.

Here we consider some possible mechanisms that can reduce the water temperature in the shelf-slope region and cause the long-term decreasing trend of oceanic heat transport.

5.2. Local Wind Effects

It is well known that surface winds can lower the sea temperature not only by air-sea turbulent heat flux but also by driving upwelling [e.g., *Tomczak and Godfrey*, 1994]. Here the effect of the surface flux is estimated so that the latter effect can be considered. Upwelling is induced by divergence of the surface Ekman

Table 3. Linear Trend and the 95% Confidence Limits of Seasonal Anomalies of $\partial OHC/\partial t$ and Net Heat Fluxes Q_{net} in the SIS (Unit: W m^{-2} yr^{-1}) and Correlation Between 7 Year Running Averaged Seasonal Anomalies of $\partial OHC/\partial t$ and Q_{net}[a]

|	$\partial OHC/\partial t$ Trend	Q_{net} Trend	Correlation
Winter	-0.13 ± 0.31	0.01 ± 0.46	**0.53**
Spring	-0.34 ± 0.26	0.40 ± 0.35	-0.07
Summer	0.10 ± 0.30	0.76 ± 0.41	**0.56**
Autumn	0.43 ± 0.30	0.48 ± 0.40	**0.82**

[a]The significant correlation coefficients are given in bold font.
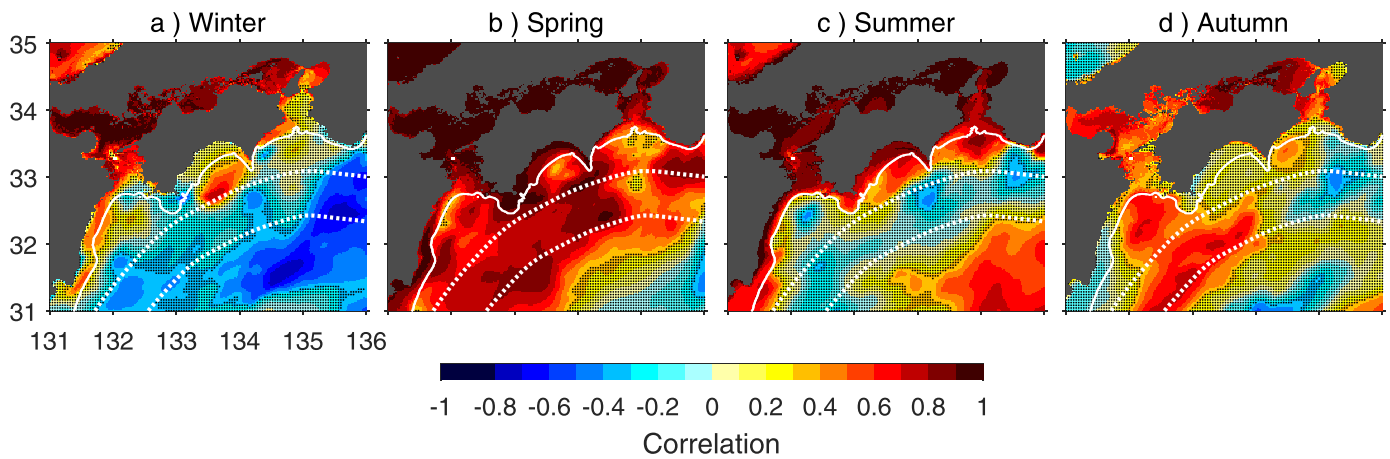
**Figure 9.** Correlation map of oceanic heat transport Q_v averaged over the whole SIS and the local value in each season. Correlations are calculated for the 7 year running mean time series. Shading is overlaid where correlation is statistically insignificant. Solid and dashed white lines in each plot are the same as those in Figures 3i–3l.

transport and therefore its generation strongly depends on the wind (stress) curl [e.g., *Tomczak and Godfrey*, 1994]. Hereinafter, we refer to such an upwelling as wind curl-driven upwelling.

Figure 12 shows the linear trend of the spring-time wind velocity (vector) and of wind speed magnitude (color shade). It is obvious that westerly wind velocity increased above the Kuroshio ($\sim$0.02 m s^{-1} yr^{-1}), while that immediately south of Shikoku Island and east of Kyushu Island was relatively small. In addition, north-westerly wind velocity increased (0.01–0.02 m s^{-1} yr^{-1}) in the western SIS and the channels (Iyo Nada and the Bungo Channel).
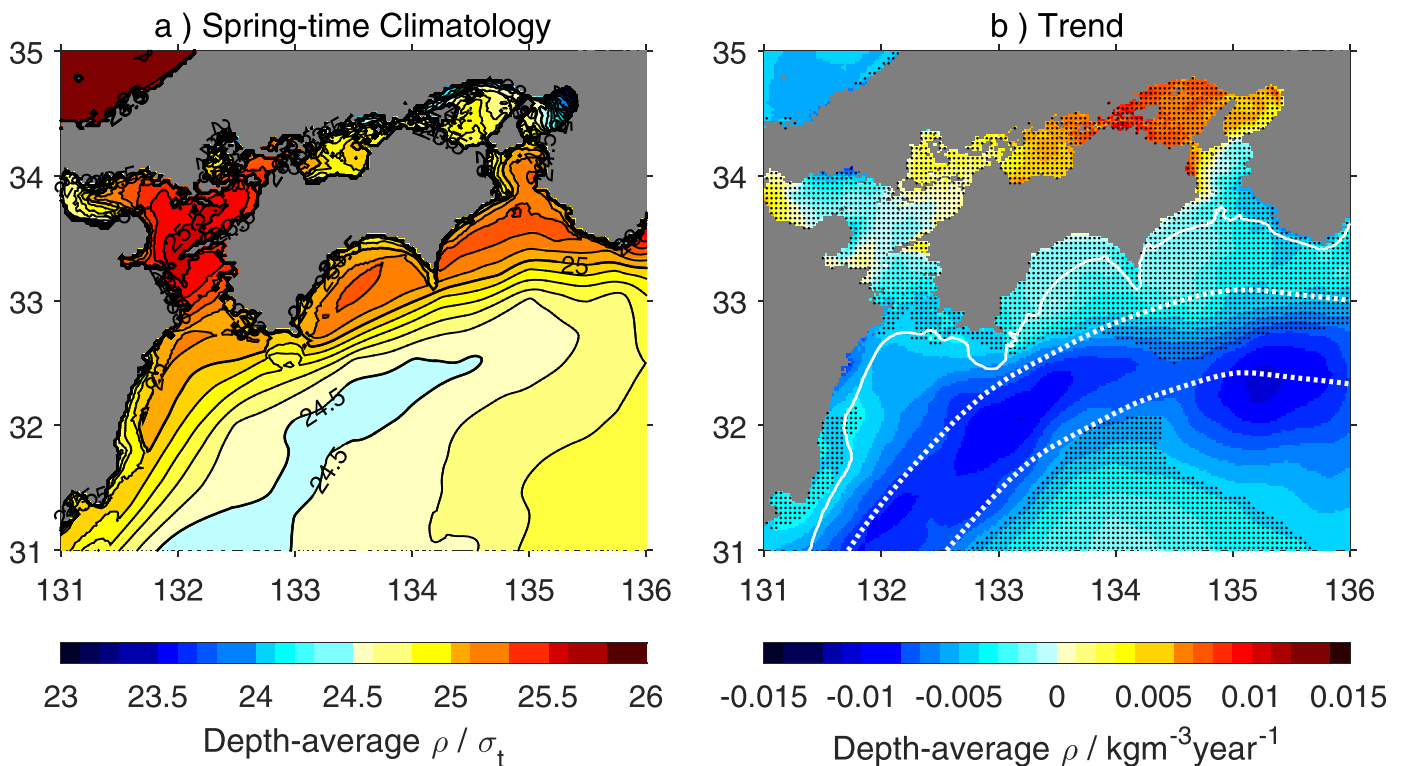
Figure 10. (a) Climatology and (b) linear trend of the spring-time depth-average potential density. In the Kuroshio region, the depth-average was taken over the upper 200 m depth. Shade, solid, and dashed white lines in the right plot are the same as in Figures 3i–3l.
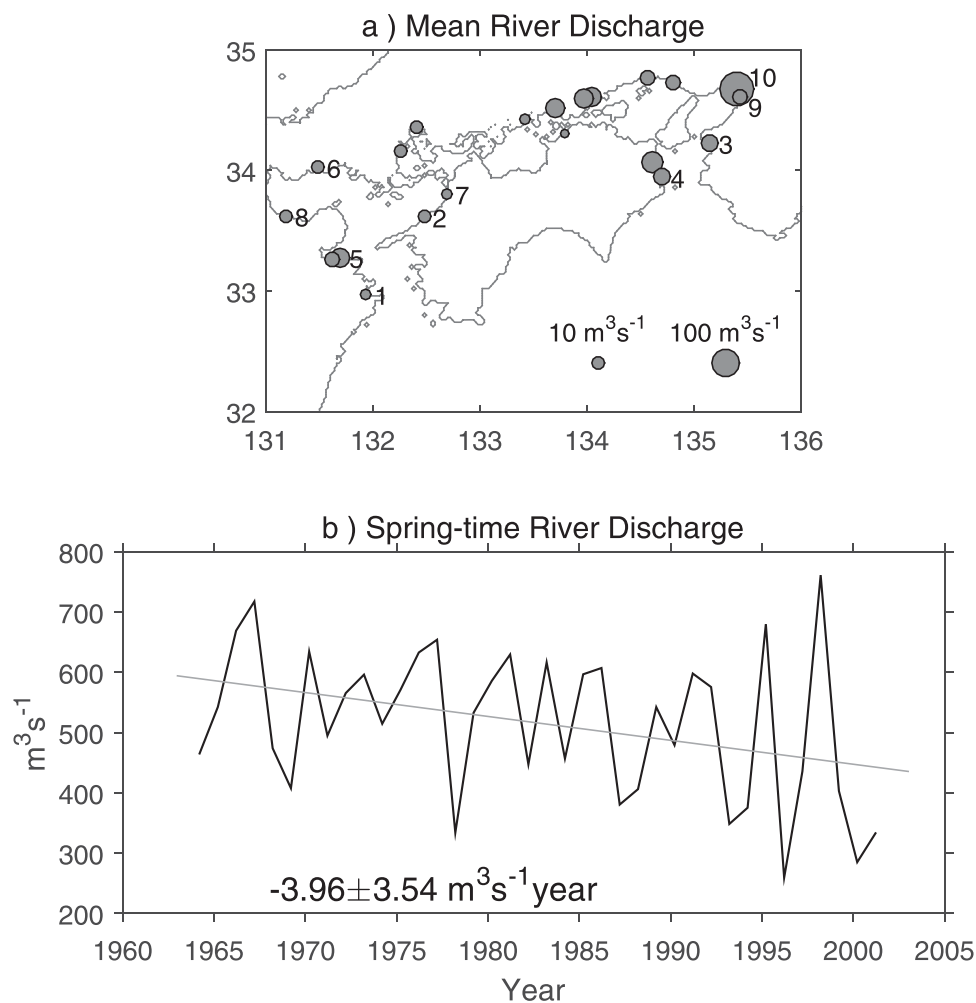
Figure 11. (a) Annual mean discharge rate of the rivers in the SIS and the channels. The area of the circles depicted at each river mouth indicate the discharge rate. (b) Interannual variation (thick line) and linear trend (thin line) of spring-time total discharge of the 10 rivers numbered in Figure 11a.

The pattern of the long-term variation in wind velocity in the Kuroshio region resulted in a systematic variation of the wind curl field: a linear trend of spring-time wind curl indicates increasing wind curl over the shelf-slope region east of 133°E (Figure 13). The linear trend of the wind curl in the shelf-slope region was typically $1–3 \times 10^{-7}$ s^{-1} yr^{-1}, which is favorable for an increase in the rate of wind curl-driven upwelling. In fact, long-term (7 year running mean) variations of the spring-time wind curl averaged over the shelf-slope region east of 133°E and the spring-time Q_v in the SIS show significant negative and positive linear trends, respectively (Figure 13b). In addition, they have a good correlation ($r = -0.60$), suggesting stronger wind curl-driven upwelling in the eastern shelf-slope region relates to weaker oceanic heat transport to the SIS.

In addition to the wind curl-driven upwelling, it would be expected that coastal upwelling had also been intensified by the enhancement of westerly wind speed whose role can be understood as a spatially constant wind stress over the shelf slope region (Figure 12a). Upwelling velocities due to wind curl-driven and coastal upwelling may be scaled by $w_e = \text{curl}\tau/(\rho_0 f)$ and $w_c = \tau_y/(\rho_0 f L)\exp(-x/L)$ respectively, where τ_y is the along-coast component of wind stress τ, f is Coriolis frequency, x is the offshore distance from the coast, and L is internal Rossby radius of deformation [*Gill*, 1982]. To estimate the relative importance of w_c to w_e, a rough estimation on linear trend of the upwelling velocities is presented here. Using spring-time wind stress, $f = 8 \times 10^{-5}$ s^{-1} and $L = 10$ km based on our data, we calculated spring-time w_e and w_c from the coast or 100 m isobaths to the northern edge of the Kuroshio and obtained their linear trend of 1.8×10^{-6} and 1.7×10^{-6} m s^{-1} yr^{-1}, respectively. Thus, coastal upwelling could have played the same role in increasing upwelling in the shelf-slope region as wind curl-driven upwelling.
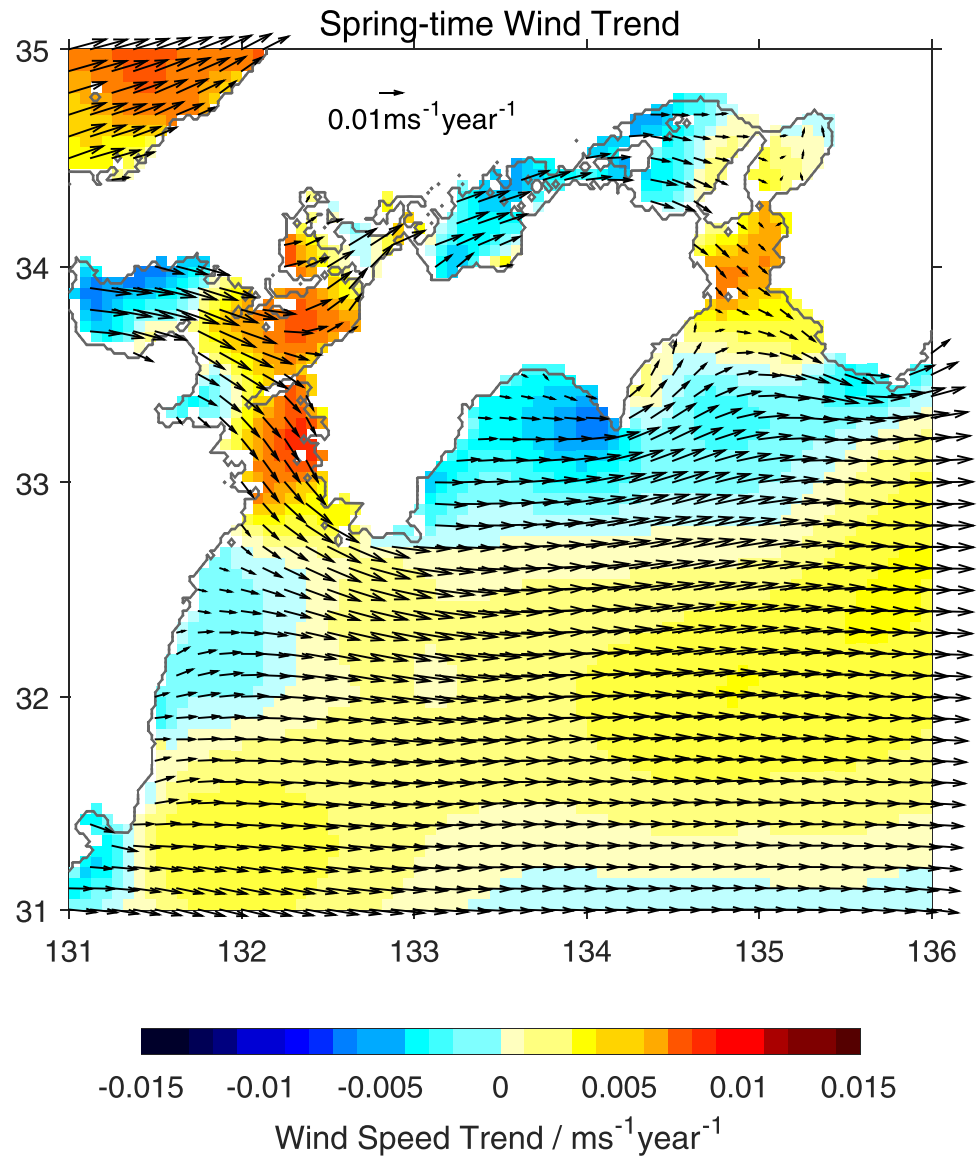
Figure 12. Linear trend of the spring-time surface wind. Color shade and quiver denote the trend of wind speed magnitude and wind vector, respectively.

The increased north-westerly wind in the western SIS and channel also could have reduced water exchange between the SIS and the shelf-slope water (Figure 12). Because spring-time oceanic heat transport in the western SIS was likely driven by the inverse-estuarine circulation (northward surface current with a counter bottom flow) as noted in section 5.1, the increased north-westerly wind should have counteracted the circulation by creating southward surface Ekman transport.

We therefore conclude the changes in the local wind field are one of the major causes for the decrease in the spring-time oceanic heat transport to the SIS.

5.3. Effect of the Kuroshio Transports

As shown in Figure 8j, a negative linear trend of the spring-time oceanic heat transport Q_v can be found not only in the SIS but also in the Kuroshio region, especially in the western part. The negative trend of the spring-time Q_v in the Kuroshio suggests that the spring-time Kuroshio heat transport has decreased. The positive correlation between the spring-time Q_v averaged over the SIS and that over the Kuroshio region
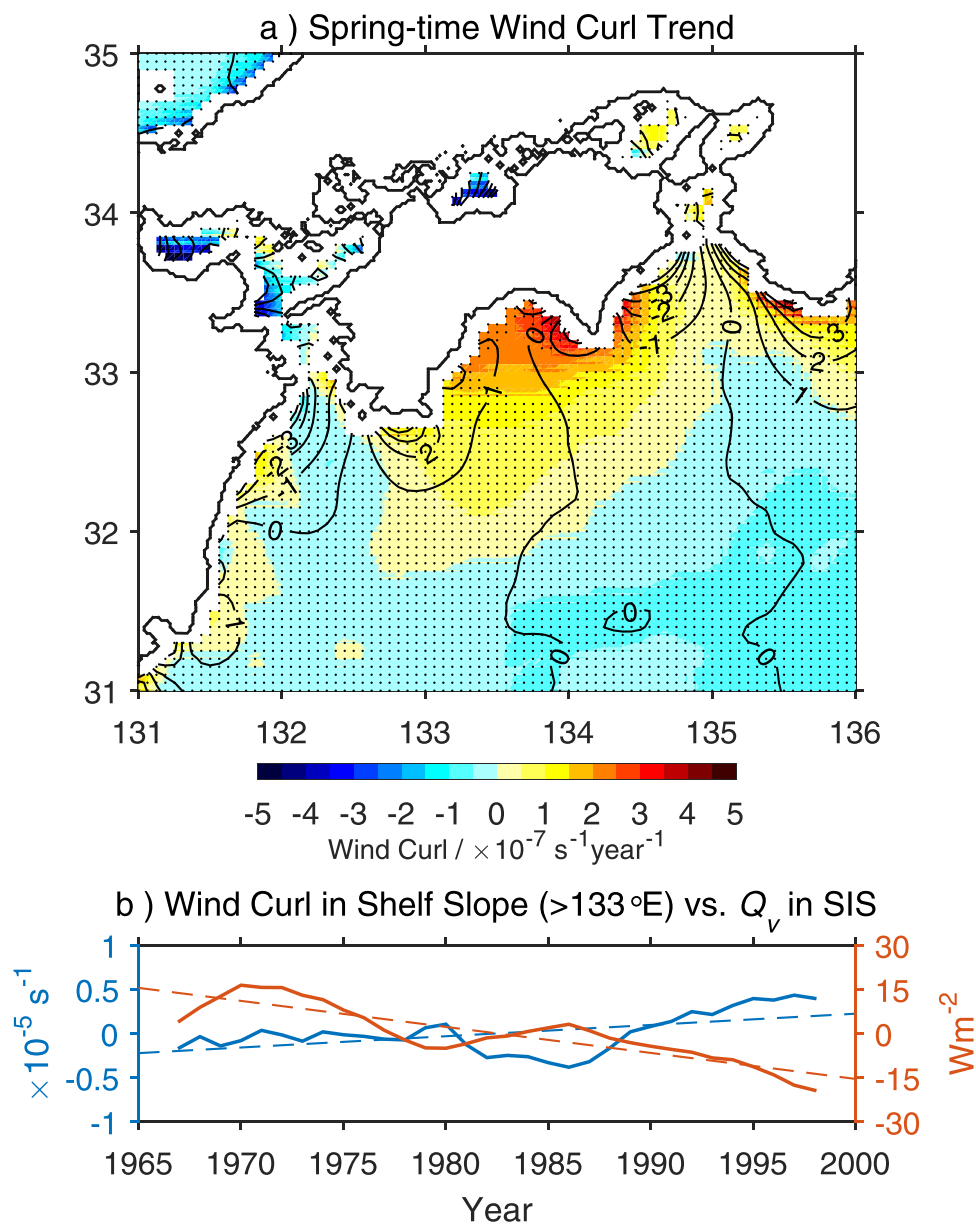
Figure 13. (a) Linear trend (color shade) and climatology (line contour in $\times 10^{-5}$ s^{-1}) of spring-time wind curl. (b) The 7 year running mean variation in the spring-time wind curl averaged over shelf-slope region east of 133°E (blue solid line) and spring-time Q_v in the SIS (red solid line). Blue and red dashed lines in the bottom plot are linear fits for the wind curl and Q_v, respectively.

($r = 0.56$) indicates the Kuroshio heat transport could be related to the decreased spring-time oceanic heat transport to the SIS.

The Kuroshio can contribute to the Q_v in the SIS through dynamical isotherm uplift, as noted in section 3.1. Because the high spring-time linear trend in water temperature in the Kuroshio (Figures 4b and 4f) indicates an increase of the Kuroshio front and therefore of the Kuroshio geostrophic (volume) transport, the associated isotherm uplift could have enhanced cold water transport to the SIS. However, high positive correlation between long-term Q_v in the SIS and in the Kuroshio region (Figure 9b) does not support the significance of this process in spring, because if the isotherm uplift played a central role in the heat transport to the SIS, a positive correlation would appear only in the shelf-slope region, not in the Kuroshio in Figure 9b. We conclude that the decrease in the spring-time Kuroshio heat transport was another major contributor to the decrease in the spring-time heat transport in the SIS.

The dynamical isotherm uplift might have contributed to the decreased summer-time Q_v in the SIS, discussed in section 4.3, because the long-term Q_v in the SIS does not correlate with that in the Kuroshio, but instead with that in the shelf-slope region (Figure 9c). This is consistent with the fact that summer-time Q_v in the SIS is due to oceanic transport of cold water from the shelf-slope region.

Mechanisms controlling the Kuroshio transport south of Shikoku are complicated. The Kuroshio volume transport is much larger south of Shikoku ($\sim$60 Sv = 10^6 m^3 s^{-1}) than in the East China Sea ($\sim$25 Sv), which is mainly due to the Kuroshio recirculation that is created by an anticyclonic gyre south of Japan [Guo et al., 2013]. In addition, Kuroshio transport south of Shikoku is also affected by westward-propagating, cyclonic mesoscale eddies and/or variation of the Kuroshio path [Tsujino et al., 2013]. These factors possibly resulted in the locality of the oceanic heat transport in the Kuroshio region south of Shikoku as well as its seasonality. In fact, the decreasing trend in the Kuroshio heat transport in the East China Sea reported by Zhang et al. [2012] was not found in this study. Investigation of the relation of Q_v to such factors is beyond the scope of this investigation because they are not fully resolved in our data sets.

5.4. Salinity Change in the SIS

As noted in section 5.1, spring-time water density in the eastern part of the SIS likely increased (Figure 10b). This also suggests a weakening of the meridional circulation in the eastern SIS. Because the spring-time water temperature in the SIS did not decrease (Figures 6c and 6h), the increase in water density is likely due to an increase in salinity (figure not shown).

The decrease in salinity in the SIS could have been caused by the decrease in freshwater input from rivers: the spring-time total discharge rate of the 10 rivers numbered in Figure 11a significantly decreased between 1964 and 2001 (-3.96 ± 3.54 m^3 s^{-1} yr^{-1}: Figure 11b). These 10 rivers were selected because data for these rivers were available for the full period considered in this investigation. The discharge rate presented in Figure 11b was fairly representative of the long-term variation for all of the rivers.

The relation of the decreased river discharge with the local atmospheric forcing (i.e., precipitation) is unclear because the spring-time total precipitation measured at the observation stations (Figure 2a) showed a large inter-annual variability and therefore insignificant linear trend (-0.4 ± 34.7 mm month^{-1} yr^{-1}). It also could have depended on other factors such as winter-time snowfall and the timing of the melting of the snow, effects of groundwater and the construction of dams.

6. Summary

Using in situ hydrographic data over the period 1964–2001, we investigated the climatology and linear trend of seasonal water temperature and heat budget in the SIS. Winter-time water temperature and ocean heat content showed significant increasing trends, while the summer-time values exhibited no significant change. By analyzing heat budget between the tendency of ocean heat content $\partial OHC/\partial t$ and air-sea net heat flux Q_{net}, the driving factor of the winter-time warming trend in the SIS was identified as autumn-time Q_{net}, while the summer-time OHC was unchanged mainly due to decreased spring-time oceanic heat transport to the SIS from the Kuroshio region, $Q_v = \partial OHC/\partial t - Q_{net}$.

We then proposed possible mechanisms for the long-term decreasing trend of spring-time heat transport. First is the increased upwelling due to divergence of surface Ekman transport induced by enhanced wind curl and wind speed in the shelf-slope region. The reduction in surface temperature in the Kuroshio region can weaken density-driven circulation in the channels responsible for the heat transport from the shelf-slope region to the SIS. Second is the heat transport by the Kuroshio south of Shikoku Island. The spring-time Kuroshio heat transport south of Shikoku Island significantly decreased and this can contribute to the oceanic heat transport in the SIS. Third is the decreased freshwater input by rivers to the SIS. This can also weaken water exchange between the SIS and the Kuroshio region.

Water temperature in the SIS is thus highly affected by both oceanic and atmospheric forcing which relates to seasonal and long-term variations as well as various spatial scales (e.g., basin scale of the Kuroshio, regional scale of wind curl and mesoscale of the recirculation gyre). Importantly, these forcings are dependent on each other. For example, summer-time low SST in the SIS affects surface wind speed [Iwasaki et al., 2015], and it can change coastal sea circulation such as estuarine circulation and therefore oceanic heat

transport. The mechanisms controlling water temperature in the SIS are therefore complex and careful consideration is necessary in predictions of the oceanic responses to future climate change on aspects of hydrographic condition, nutrient supplement, coastal ecosystem, and so on.

Appendix A: Definition of the Path and Edges of the Kuroshio

For identification of the location of the Kuroshio, we used the Kuroshio Current Axis Dataset 1955–2006 by the Marine Information Research Center in Japan Hydrographic Association. The data set generally provides weekly or biweekly longitude and latitude of the path of the Kuroshio south of Japan from 1955 to 2006. In the data set, the path of the Kuroshio is determined as follows. The northern edge of the Kuroshio is first estimated from horizontal distributions of the in situ sea surface temperature, 200 m depth temperature and surface current velocity, location of a specific cold eddy and satellite altimetry data (if available). Then, the path and southern edge of the Kuroshio are determined as locations at distances of 24.6 and 73.9 km from the northern edge to cross-stream direction, respectively.

References

Bao, B., and G. Ren (2014), Climatological characteristics and long-term change of SST over the marginal seas of China, *Cont. Shelf Res.*, *77*, 96–106.

Belkin, I. M. (2009), Rapid warming of large marine ecosystems, *Prog. Oceanogr.*, *81*, 207–213.

Belkin, I. M., and M.-A. Lee (2014), Long-term variability of sea surface temperature in Taiwan Strait, *Clim. Change*, *124*, 821–834.

Book, J. W., M. Wimbush, S. Imawaki, H. Ichikawa, H. Uchida, and H. Kinoshita (2002), Kuroshio temporal and spatial variations south of Japan determined from inverted echo sounder measurements, *J. Geophys. Res.*, *107*(C9), 3121, doi:10.1029/2001JC000795.

Bretherton, F. P., R. E. Davis, and C. B. Fandry (1976), A technique for objective analysis and design of oceanographic experiments applied to MODE-73, *Deep Sea Res. Oceanogr. Abstr.*, *23*, 559–582.

Chang, P. H., X. Guo, and H. Takeoka (2009), A numerical study of the seasonal circulation in the Seto Inland Sea, Japan, *J. Oceanogr.*, *65*, 721–736.

Clark, N. E., L. Eber, R. M. Laurs, J. A. Renner, and J. F. T. Saur (1974), Heat exchange between ocean and atmosphere in the eastern North Pacific for 1961-71, *NOAA Tech. Rep. NMFS SSRF-682*, U. S. Dep. of Commer., Washington, D. C.

Gill, A. E. (1982), *Atmosphere-Ocean Dynamics*, 662 pp., Academic, London, U. K.

Guo, X. Y., X.–H. Zhu, Y. Long, and D. J. Huang (2013), Spatial variations in the Kuroshio nutrient transport from the East China Sea to south of Japan, *Biogeosciences*, *10*, 6403–6417.

Hickox, R., I. Belkin, P. Cornillon, and Z. Shan (2000), Climatology and seasonal variability of ocean fronts in the East China, Yellow and Bohai Seas from satellite SST data, *Geophys. Res. Lett.*, *27*, 2945–2948.

Hirose, N., H.-C. Lee, and J.-H. Yoon (1999), Surface heat flux in the East China Sea and the Yellow Sea, *J. Phys. Oceanogr.*, *29*, 401–417.

Ishizaki, H., and M. Saito (1978), On the evaporation amount in the Seto Inland Sea [in Japanese], *Bull. Coastal Oceanogr.*, *16*, 11–20.

Iwasaki, S., A. Isobe, and Y. Miyao (2015), Fortnightly atmospheric tides forced by spring and neap tides in coastal waters, *Scientific Reports*, *5*, 10167, doi:10.1038/srep10167.

Johnson, D. R., and T. P. Boyer (2015), *Regional Climatology of the East Asian Seas: An Introduction, NOAA Atlas NESDIS 79*, 37 pp., National Centers for Environmental Information, U.S. Department of Commerce, Silver Spring, Md., doi:10.7289/V5D21VM9.

Kakinoki, K., S. Imawaki, H. Uchida, H. Nakamura, K. Ichikawa, S. Umatani, A. Nishina, H. Ichikawa, and M. Wimbush (2008), Variations of Kuroshio geostrophic transport south of Japan estimated from long-term IES observations, *J. Oceanogr.*, *64*, 373–384.

Kida, S., et al. (2015), Oceanic fronts and jets around Japan—A review, *J. Oceanogr.*, *71*, 469–497.

Kobayashi, S., et al. (2015), The JRA-55 reanalysis: General specifications and basic characteristics, *J. Meteorol. Soc. Jpn.*, *93*, 5–48.

Kondo, A., A. Isobe, and M. Shinohara (2005), Long-term variations of water temperature in Fukuoka Bay and their possible cause [in Japanese with English abstract], *J. Oceanogr. Soc. Jpn.*, *14*(3), 339–409.

Kondo, J. (1975), Air–sea bulk transfer coefficients in diabatic conditions, *Boundary Layer Meteorol.*, *9*, 91–112.

Kondo, J. (1976), Heat balance of the East China Sea during the Air Mass Transformation Experiment, *J. Meteorol. Soc. Jpn.*, *54*, 382–398.

Lima, F. P., and D. S. Wethey (2012), Three decades of high-resolution coastal sea surface temperatures reveal more than warming, *Nat. Commun.*, *3*, 1–13.

Liu, N., C. Eden, H. Dietze, D. Wu, and X. Lin (2010), Model-based estimate of the heat budget in the East China Sea, *J. Geophys. Res.*, *115*, C08026, doi:10.1029/2009JC005869.

Miyazawa, Y., X. Guo, and T. Yamagata (2004), Roles of mesoscale eddies in the Kuroshio path, *J. Phys. Oceanogr.*, *34*, 2203–2222.

Murakami, M., Y. Oonishi, and H. Kunishi (1989), Heat and salt balances in the Seto inland sea, *J. Oceanogr. Soc. Jpn.*, *45*, 204–216.

Qiu, B., and W. Miao (2000), Kuroshio path variations south of Japan: Bimodality as a self-sustained internal oscillation, *J. Phys. Oceanogr.*, *30*, 2124–2137.

Rhein, M., et al. (2013), Observations: Ocean, in *Climate Change 2013: The Physical Science Basis. Contribution of Working Group I to the Fifth Assessment Report of the Intergovernmental Panel on Climate Change*, edited by T. F. Stocker et al., Cambridge Univ. Press, Cambridge, U. K.

Senjyu, T., I.-S. Han, and S. Matsui (2010), Interdecadal variations of temperature and salinity structures in the Tsushima Strait, *Pac. Oceanogr.*, *5*, 44–55.

Shen, M. L., Y.-H. Tseng, and S. Jan (2011), The formation and dynamics of the cold-dome off northeastern Taiwan, *J. Mar. Syst.*, *86*, 10–27.

Smith, N. R. (1995), An improved system for tropical ocean subsurface temperature analyses, *J. Atmos. Oceanic Technol.*, *12*, 850–870.

Stewart, R. (2008), Introduction to Physical Oceanography, Dep. of Oceanogr., Tex. A&M Univ., College Station, Tex.

Sugimatsu, K., and A. Isobe (2010), Intrusion of Kuroshio-derived bottom cold water into Osaka Bay and its possible cause, *J. Oceanogr.*, *66*, 191–199.

Sugimoto, S., and M. Hanawa (2014), Influence of Kuroshio oath variation south of Japan on formation of subtropical mode water, *J. Phys. Oceanogr.*, *44*, 1065–1077.

Takahashi, S., and S. Seiki (2004), Long-term change of water temperature in the Seto Inland Sea [in Japanese with English abstract], *Umi Sora*, *80*, 69–72.

Takashige A., T. Takahashi, H. Nakata, and S. Kimura (2013), Long-term trends in sea surface temperature in coastal water in relation to large-scale climate change: A case study in Omura Bay, Japan, *Cont. Shelf Res.*, *66*, 73–82.

Takeoka, H., O. Matsuda, and T. Yamamoto (1993), Processes causing the chlorophyll a maximum in the tidal front in Iyo-Nada, Japan, *J. Oceanogr.*, *49*, 57–70.

Takeoka, H., A. Kaneda, and H. Anami (1997), Tidal fronts induced by horizontal contrast of vertical mixing efficiency, *J. Oceanogr.*, *53*, 563–570.

Takeoka, H., Y. Hayami, and A. Kaneda (2005), Long term variations in the marine environments of the Seto Inland Sea [in Japanese with English Abstract], *Bull. Coastal Oceanogr.*, *43*, 45–50.

Tawara, S., (1986), Studies on the characteristics of oceanographic conditions in relation to fishing condition in the shallow coastal waters [in Japanese with English Abstract], *J. Shimonoseki Univ. Fish.*, *34*, 1–103.

Tomczak, M., and J. S. Godfrey (1994), *Regional Oceanography: An Introduction*, 442 pp., Pergamon, Oxford, U. K.

Tsujino, H., S. Nishikawa, K. Sakamoto, N. Usui, H. Nakano, and G. Yamanaka (2013), Effects of large-scale wind on the Kuroshio path south of Japan in a 60-year historical OGCM simulation, *Clim. Dyn.*, *41*, 2287–2318.

Valle-Levinson, A. (Ed.) (2010), *Contemporary Issues in Estuarine Physics*, 326 pp., Cambridge Univ. Press, Cambridge, U. K.

Wu, L., et al. (2012), Enhanced warming over the global subtropical western boundary currents, *Nat. Clim. Change*, *2*(3), 161–166.

Yanagi, T. (1987), Classification of "Siome", Streaks and Fronts, *J. Oceanogr. Soc. Jpn.*, *45*, 149–158.

Zhang, Q., Y. Hou, and T. Yan (2012), Inter-annual and inter-decadal variability of Kuroshio heat transport in the East China Sea, *Int. J. Climatol.*, *32*, 481–488, doi:10.1002/joc.2295.